Patch Matching-Based Multitemporal Group Sparse Representation for the Missing Information Reconstruction of Remote-Sensing Images

Article *in* IEEE Journal of Selected Topics in Applied Earth Observations and Remote Sensing · January 2016

Impact Factor: 3.03 · DOI: 10.1109/JSTARS.2016.2533547

4 authors, including:

Xinghua Li

Wuhan University

11 PUBLICATIONS **41** CITATIONS

SEE PROFILE

Huifang Li

Wuhan University

13 PUBLICATIONS **71** CITATIONS

SEE PROFILE

Patch Matching-Based Multitemporal Group Sparse Representation for the Missing Information Reconstruction of Remote-Sensing Images

Xinghua Li, *Student Member, IEEE*, Huanfeng Shen, *Senior Member, IEEE*, Huifang Li, *Member, IEEE*, and Liangpei Zhang, *Senior Member, IEEE*

***Abstract*—Poor weather conditions and/or sensor failure always lead to inevitable information loss for remote-sensing images acquired by passive sensor platforms. This common issue makes the interpretation (e.g., target recognition, classification, change detection) of remote-sensing data more difficult. Toward this end, this paper proposes to reconstruct the missing information of optical remote-sensing data by patch matching-based multitemporal group sparse representation (PM-MTGSR). In the framework of sparse representation, the basic idea is to utilize the local correlations in the temporal domain and the nonlocal correlations in the spatial domain. Based on image patches, the local correlations are first taken into consideration. The similar patches are then grouped for joint sparse representation so that the nonlocal correlations are also considered. Owing to the patch matching of similar patches, the nonlocal correlations in the remote-sensing images are efficiently exploited. Simulated and real-data experiments demonstrate that the proposed method is effective both qualitatively and quantitatively.**

***Index Terms*—Cloud removal, group sparse representation (GSR), missing information reconstruction, nonlocal similarity, patch matching, remote sensing, spectral, temporal.**

I. Introduction

MISSING information is very common in optical remote-sensing images. The problem originates from two aspects. On the one hand, due to the harsh environment and sensor aging, onboard imagers are subject to a risk of failure. Once an imager suffers from a failure, the corresponding ground information cannot be acquired as usual (resulting in the so-called missing information). For example, the majority of the detectors (in band 6) of the moderate resolution imaging spectroradiometer (MODIS) sensor onboard the Aqua satellite are nonfunctional [1], and the scan line corrector (SLC) of the Landsat-enhanced thematic mapper plus (ETM+) sensor has permanently failed [2]. On the other hand, when the weather is cloudy or rainy, thick clouds often obscure the land surface, which also results in missing information in optical remote-sensing images. According to an approximate estimation, about 35% of the Earth's surface is covered by clouds at any one time [3]. Since information loss is an inevitable issue for optical remote-sensing images, taking reasonable measures to reconstruct the missing information can have a positive impact on the usability of the images themselves.

In the past few decades, a series of missing information reconstruction methods for remote-sensing images have been proposed, which can be grouped into four classes: 1) spatial methods, 2) spectral methods, 3) temporal methods, and 4) hybrid methods. The spatial methods make use of the local or nonlocal spatial correlations to complete the missing information and include all the different kinds of interpolation methods (e.g., nearest neighbor interpolation, bilinear interpolation, and kriging interpolation) [4], the diffusion-based methods [5], [6], the variation-based methods [7], [8], and the exemplar-based methods [9]. The spatial methods are the most basic class of the four classes. However, due to the absence of sufficient complementary information, spatial methods cannot reconstruct a large missing area. For instance, NASA uses bilinear interpolation to reconstruct Aqua MODIS band 6, and the results show obvious discontinuities between the reconstructed and good regions.

In the second class of methods, the spectral correlations lay a foundation for reconstructing large-area missing information. The most typical examples of the spectral methods are designed for use with Aqua MODIS band 6. In order to reconstruct the missing information of band 6, Rakwatin *et al.* [10] and Shen *et al.* [11] proposed to model the spectral relationship between band 6 and band 7 based on the good detectors, and, finally, the missing information is recovered according to the modeled relationship. Similarly, Gladkova *et al.* [12] and Li *et al.* [13] modeled the relationships between band 6 and all the other six bands. Additionally, Shen *et al.* [1] exploited compressed sensing theory to sparsely represent the spectral

Manuscript received August 26, 2015; revised December 21, 2015; accepted February 19, 2016. This work was supported in part by the National High Technology Research and Development Program of China (863 Program) under Grant 2013AA12A301, in part by the National Natural Science Foundation of China (NSFC) under Grant 41422108 and Grant 41401396, in part by the Cross-disciplinary Collaborative Teams Program for Science, Technology and Innovation of the Chinese Academy of Sciences, and in part by the Fundamental Research Funds for the Central Universities of China under Grant 2014205020201. *(Corresponding author: Huanfeng Shen.)*

X. Li and H. Li are with the School of Resource and Environmental Sciences, Wuhan University, Wuhan 430079, China (e-mail: lixinghua5540@whu.edu.cn; huifangli@whu.edu.cn).

H. Shen is with the School of Resource and Environmental Sciences, Wuhan University, Wuhan 430079, China, and with the Key Laboratory of Geographic Information System, Ministry of Education, Wuhan University, Wuhan 430079, China, and also with the Collaborative Innovation Center for Geospatial Information Technology, Wuhan University, Wuhan 430079, China (e-mail: shenhf@whu.edu.cn).

L. Zhang is with the State Key Laboratory of Information Engineering in Surveying, Mapping, and Remote Sensing, Wuhan University, Wuhan 430079, China, and also with the Collaborative Innovation Center for Geospatial Information Technology, Wuhan University, Wuhan 430079, China (e-mail: zlp62@whu.edu.cn).

Color versions of one or more of the figures in this paper are available online at http://ieeexplore.ieee.org.

Digital Object Identifier 10.1109/JSTARS.2016.2533547

correlations between band 6 and the other bands, and the effect was satisfactory. By further exploiting the spectral correlations, the result was better than when only using one extra spectral band. There have also been a number of studies of cloud removal based on spectral correlations. For an optical remote-sensing image contaminated by cloud, it is quite difficult to remove the clouds in the visible spectrum. As a result, most researchers have resorted to extracting complementary information from the infrared spectrum, which penetrates clouds more powerfully than the visible spectrum. For example, Wang *et al.* [14] used wavelet analysis to remove the clouds in the infrared spectrum and then reconstructed the cloudy area of the visible spectrum by a B-spline-based model. Using an improved homomorphic filtering method, Chun *et al.* [15] filtered out clouds according to the statistical characteristics of the image information, in which the clouds are considered as noise. Li *et al.* [16] removed thin cloud in the visible spectrum using a fusion of the visible and short-wave infrared spectra.

The third class is the temporal methods, which have attracted the most attention for missing information reconstruction, especially cloud removal. The most basic method is missing information replacement from another time, including both direct and indirect replacements. Direct replacement involves selecting the optimal value in a time series [3], [17], (e.g., the maximum value composite (MVC) procedure [18]); indirect replacement involves first reducing the temporal differences between the degraded image and the auxiliary images and then replacing the missing information as the direct replacement does [3], [19]–[22]. However, such temporal replacement may neglect the normal changes of the underlying surfaces over time, amounting to a reduction in the temporal resolution. Temporal interpolation is another kind of method, for which the geostatistical methods (e.g., cokriging) are representative [23]–[25]. When a time series is long enough, a large number of scholars favor the temporal filter methods, which include the sliding window filter (e.g., the best index slope extraction method [26] and the Savitzky–Golay filter [27]), function-based curve fitting (e.g., the asymmetric Gaussian model [28] and double logistic model [29]), and the frequency domain methods (e.g., the harmonic analysis of time series (HANTS) [30]). In general, a temporal filter has a more powerful ability to keep the dynamic variation of ground features than temporal replacement. However, to some degree, temporal filters still reduce the temporal resolution of remote-sensing images. More recently, with the advent of sparse representation, a number of new algorithms have been developed. Lorenzi *et al.* [31] considered cloud removal as a multiobjective genetic optimization scheme under the perspective of compressed sensing. Li *et al.* proposed two algorithms based on a synthesis model [32] and an analysis model [33], and these two models can obtain satisfactory results on the premise of a series of multitemporal data. It is, however, noteworthy that all the temporal methods are powerless with regard to the abrupt transformation of geographical objects (e.g., new buildings and man-made landscapes) [34].

The above-mentioned three classes of methods make use of the spatial correlations, the spectral correlations, or the temporal correlations in remote-sensing images. However, they do not synthetically exploit all three kinds of correlations. To this end, hybrid methods have been proposed which integrate two or three kinds of correlations. Benabdelkader and Melgani [35] opportunely captured the spatial and spectral correlations by postreconstruction of the contextual process. For Landsat SLC-off images, Zeng *et al.* [2] used indirect temporal replacement to first complete the main missing information and then used a variational method in the spatial domain to complete the remainder. Cheng *et al.* [36] obtained the statistical information of similar pixels according to an auxiliary image from another time (temporal domain), which guides the cloud removal in the spatial domain. Li *et al.* [33] proposed to utilize the spectral and temporal correlations in the framework of sparse representation. However, the similarity between patches is ignored in the reconstruction process. Recently, Zhang *et al.* [37] proposed the group sparse representation (GSR) for digital image restoration based on patch similarity. Inspired by this approach, this paper makes the best use of the local sparsity in the temporal domain and the nonlocal similarity in the spatial domain to reconstruct the missing information of remote-sensing images. First, the temporal differences are reduced by normalization of the auxiliary images. The similar patches are then grouped and matched with the target patch. Finally, sparse representation is applied to complete the missing information. The proposed method is called patch matching-based multitemporal group sparse representation (PM-MTGSR). However, another kind of GSR approach was proposed in [38], [39], and compared with these methods, PM-MTGSR groups the similar patches, rather than the similar atoms of a learned dictionary. In summary, this paper has two main contributions: 1) the GSR is expanded from the spatial domain (of a digital image) to the temporal domain (of a remote-sensing image); 2) the idea of patch matching is introduced into the framework of GSR.

This paper is organized as follows. In Section II, we introduce the PM-MTGSR method from the aspects of image normalization, similar patch search, patch matching, and missing information reconstruction. This is followed by the missing information reconstruction experiments in Section III. The corresponding conclusion is drawn in Section IV.

II. PM-MGSR Method

Since the hybrid methods have more advantages in missing information reconstruction than the other three kinds of method, this paper proposes to simultaneously combine the spatial and temporal correlations in the framework of GSR. By utilizing the temporal correlations, the proposed method obtains the prior information of the missing areas in the remote-sensing images. Thanks to the spatial correlations, the similar patches to the target patch are found and grouped into a set which can then be sparsely represented. The similar patches are then matched with the target patch in a group. After patch matching, the correlations of the grouped patches are strengthened. The integral process of the proposed PM-MTGSR method consists of four parts: 1) image normalization; 2) similar patch search; 3) patch matching; and 4) missing information reconstruction. We give a detailed description of the process in Sections II-A–D.

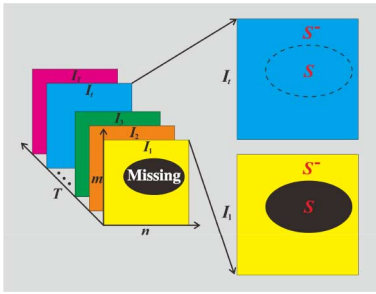

Fig. 1. Multitemporal remote-sensing images with both missing and good areas.

A. Image Normalization

Since the shooting angle, imaging time, and atmospheric environment are usually different, multitemporal remote-sensing images over the same geographical area show obvious radiance differences. As a result, temporal differences are common in multitemporal images. These differences seriously affect the utilization of the temporal correlations in the reconstruction process and hinder us from trying to find similar patches. To reduce this kind of harmful influence, image normalization is adopted.

For the convenience of description, we suppose that all the used remote-sensing images are two dimensional. Given a series of remote-sensing images $\{I_t\}_{t=1}^{T} \in \mathbb{R}^{m\times n}$, each I_t can be a component of a multitemporal or multispectral image. For example, I_1, I_2, and I_3 can be acquired from three periods over the same geographical area (multitemporal), and they can also be the red, green, and blue bands (or other spectral bands) simultaneously acquired from the same geographical area (multispectral). Without loss of generality, as shown in Fig. 1, I_1 consists of missing region S and good region S^-, and the other good $\{I_t\}_{t=2}^{T}$ also consist of the corresponding two regions S and S^-. It is noteworthy that the regions S and S^- of $\{I_t\}_{t=2}^{T}$ are good regions. Hereafter, I_1 is called the target image and the others are called the auxiliary images. Similarly, S is called the target region, and S^- is called the reference region. In order to quantify the difference between the target image and auxiliary images, they are supposed to satisfy the following equation:

$$I_1\left(S \cup S^-\right) = a_t I_t\left(S \cup S^-\right) + b_t, \quad t = 2, 3, \ldots, T \quad (1)$$

where $I_t\left(S \cup S^-\right)$ denotes the pixels belonging to region $S \cup S^-$ of I_t, and a_t and b_t are the regression parameters. In fact, each pair of a_t and b_t is solved by the least-squares method [33] according to the reference regions of the target and auxiliary images, as follows:

$$I_1\left(S^-\right) = a_t I_t\left(S^-\right) + b_t, \quad t = 2, 3, \ldots, T. \quad (2)$$

Once a_t and b_t are solved, they are applied to normalize the auxiliary images

$$J_t\left(S \cup S^-\right) = a_t I_t\left(S \cup S^-\right) + b_t, \quad t = 2, 3, \ldots, T \quad (3)$$

where J_t is the normalized version of I_t.

The previous normalization is imposed on the auxiliary images directly. However, in direct normalization, only one pair of regression parameters for one auxiliary image may cause a large fitting error. Researchers have shown that direct normalization is better conducted in a local window. When the classification map of the auxiliary image is available, within-class fitting [11] or local within-class fitting [40] can be adopted in the normalization process. The local within-class fitting corresponds to undertaking the normalization in a local window. As is well known, when the temporal difference is not obvious for multitemporal images, within-class normalization is better; when the temporal difference is obvious, direct normalization is better. How the different sizes of window can influence the reconstruction result is discussed in the experimental section.

B. Similar Patch Search

As stated previously, one of the reasons for image normalization is to improve the search for similar patches, which will be grouped into one set thereafter. However, before searching for similar patches, some other preprocessing steps are required. Since all the missing information reconstruction methods can be generalized as estimating the missing values according to the good values (in the reference region), a number of researchers have tended to only exploit the good values, including in the similar patch search. Nevertheless, this paper favors searching for the similar patches based on target and reference regions. For this purpose, the target region is initially completed by the nearest neighbor interpolator. However, no matter which spatial interpolator is applied, it will achieve an unsatisfactory effect when the target region is large. On that account, we propose to make use of the temporal correlations from the auxiliary images. The basic idea is that these images are permutated from three dimensions to two dimensions so that the size of the consecutive interpolated region is artificially reduced. Therefore, the interpolation accuracy can be improved, especially for a large missing area. This permutation is called "image interleaved by line" (IIL). In other words, it involves encoding the three-dimensional (3-D) sequential images line by line (the same lines of all the images constitute a tile), as shown in Fig. 2. In Fig. 2, taking three images from different periods, e.g., all the same rows of the three images consist of a tile. After this permutation, it can be easily seen that the maximum consecutive line number to be interpolated is usually one. On the basis of permutation, the missing pixels are interpolated by the nearest neighbor interpolation, as shown in Fig. 2. In fact, this way amounts to the interpolation in the temporal domain.

Fig. 3 shows the process of similar patch search after the permutation and initial interpolation. The red square represents the current target patch, and the similar patches are searched for in the surrounding window with the half size of r. By the metric of the similarity indicator between the target patch and the other patches, a similar patch is found when the indicator reaches a certain condition. The condition may be a fixed number of similar patches or an indicator threshold. In other words, the most similar patches will consist of a group, on which sparse representation is then exerted. When the similarity threshold is used, we call this the "adaptive approach." To save time, we also require that the number of similar patches should not be more than 20 in the adaptive method framework. For ease

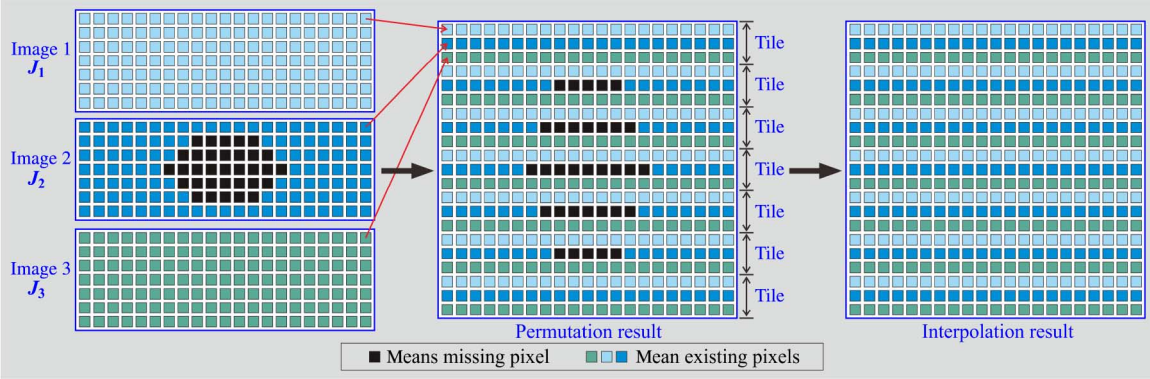

Fig. 2. Image permutation from 3-D to 2-D by IIL.

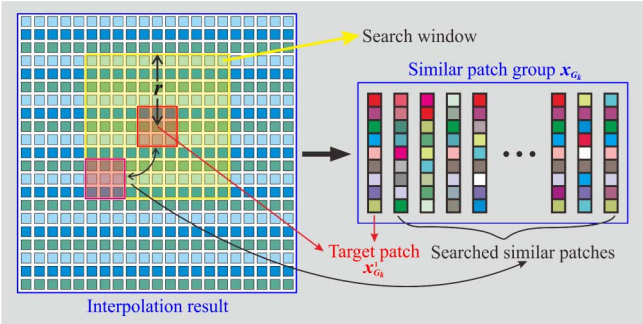

Fig. 3. Similar patch search.

of calculation, all the patches involved in the process are column stacked (that is to say, all the patches are transformed into vectors of equal length). There have been a lot of similarity indicators developed for measuring two vectors; here, we briefly introduce several of the representative methods. Given two vectors c and d with the length of l, most of the similarity indicators can be categorized into the following two groups of methods.

1) *The lower the better:* The Euclidean distance Q_E, the Jeffreys and Matusita distance Q_{JM} [41], the Canberra distance Q_{Can} [42], the mean absolute error (MAE) Q_{MAE}, and the mean relative error (MRE) Q_{MRE} (supposing d_i is the standard vector) are calculated by (4)–(8), respectively

$$Q_E = \sqrt{\sum_{i=1}^{l} (c_i - d_i)^2} \tag{4}$$

$$Q_{JM} = \sqrt{\sum_{i=1}^{l} \left(\sqrt{c_i} - \sqrt{d_i}\right)^2} \tag{5}$$

$$Q_{Can} = \sum_{i=1}^{l} \frac{|c_i - d_i|}{|c_i| + |d_i|} \tag{6}$$

$$Q_{MAE} = \sum_{i=1}^{l} |c_i - d_i| \tag{7}$$

$$Q_{MRE} = \sum_{i=1}^{l} \frac{|c_i - d_i|}{|d_i|}. \tag{8}$$

2) *The higher the better:* For all the previous indicators, a lower value means that the vectors are more similar. As far as the following indicators are concerned, a higher value means a better similarity. Correlation coefficients (CC) Q_{CC}, cosine coefficients Q_{Cos}, generalized Dice coefficients Q_{GD} [43], and generalized Jaccard coefficients Q_{GJ} [44] are calculated by (9)–(12), respectively

$$Q_{CC} = \frac{\sum_{i=1}^{l} (c_i - \mu_c)(d_i - \mu_d)}{\sqrt{\sum_{i=1}^{l} (c_i - \mu_c)^2} \sqrt{\sum_{i=1}^{l} (d_i - \mu_d)^2}} \tag{9}$$

where μ_c and μ_d are the mean values of c and d, respectively

$$Q_{Cos} = \left(\sum_{i=1}^{l} c_i d_i\right) \Big/ \sqrt{\sum_{i=1}^{l} {c_i}^2 \bullet \sum_{i=1}^{l} {d_i}^2} \tag{10}$$

$$Q_{GD} = \left(2\sum_{i=1}^{l} c_i d_i\right) \Big/ \left(\sum_{i=1}^{l} c_i^2 + \sum_{i=1}^{l} d_i^2\right) \tag{11}$$

$$Q_{GJ} = \left(\sum_{i=1}^{l} c_i d_i\right) \Big/ \left(\sum_{i=1}^{l} c_i^2 + \sum_{i=1}^{l} d_i^2 - \sum_{i=1}^{l} c_i d_i\right). \tag{12}$$

In Section III, we evaluate the impact of these indicators on the reconstruction result.

C. Patch Matching

In the framework of GSR, each target patch corresponds to a similar group. The general approach is to learn a sparse representation for this group and average the patches by the number of times they are overlapped (because one patch may belong to several groups), as in [37], [45], and [46]. In most cases, the weighted average can contribute to a good reconstruction. However, it also gives rise to a smoothing effect, which can be seen in almost all the methods based on averaging. To alleviate this effect, we just reconstruct the target patch, with the other similar patches abandoned in the final result. Additionally, in order to enhance the correlations between the target patch and similar patches, we propose to make the similar patches match the target patch (in the same group) with linear transformation, as shown in Fig. 4. We assume that the patch is of a size

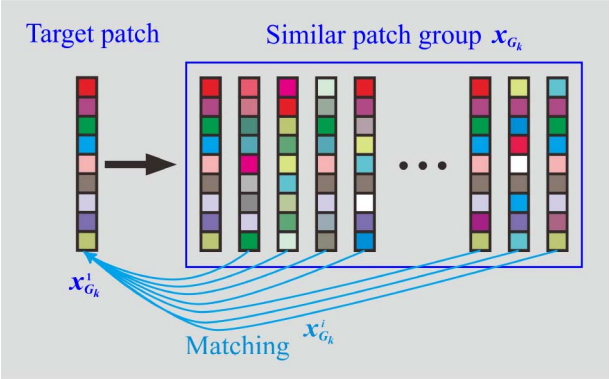

Fig. 4. Patch matching.

of $\sqrt{B} \times \sqrt{B}$, and the target patch $x_k \in \mathbb{R}^{B\times 1}$ corresponds to the group $x_{G_k} \in \mathbb{R}^{B\times g}$ (g represents the number of similar patches). We let x_k denote the extracted patch at location k from the lexicographically stacked representation of the images after interpolation ($x \in \mathbb{R}^{mnT\times 1}$), and the mathematical expression is

$$x_k = p_k(x), \quad k = 1, 2, \ldots, K \tag{13}$$

with

$$K = \frac{\left(mT - \sqrt{B} + w\right)\left(n - \sqrt{B} + w\right)}{w^2} \tag{14}$$

where $p_k(\bullet)$ represents the patch extraction operator at location k, K is the total number of extracted target patches, and w is the sliding step size on the 2-D version of x. Similarly

$$x_{G_k} = p_{G_k}(x), \quad k = 1, 2, \ldots, K \tag{15}$$

where p_{G_k} represents the operator of the similar patch group extraction at location k. Additionally, $x^i_{G_k}$ denotes the ith column of x_{G_k}. For brevity, we let $x^1_{G_k}$ be the target patch ($x^1_{G_k} = x_k$). The following linear relationship is assumed:

$$x^1_{G_k} = e_i x^i_{G_k} + f_i, \quad i = 2, 3, \ldots, g \tag{16}$$

where e_i and f_i are the parameters obtained by a linear least-squares regression. Then, $x^i_{G_k}$ is matched with $x^1_{G_k}$ by

$$\left(x^i_{G_k}\right)^{\text{new}} = e_i x^i_{G_k} + f_i, \quad i = 2, 3, \ldots, g \tag{17}$$

where $\left(x^i_{G_k}\right)^{\text{new}}$ is the new version of $x^i_{G_k}$ after patch matching.

With the patch matching completed, the missing information reconstruction with PM-MTGSR starts, which is introduced in the next section.

D. Missing Information Reconstruction

The basic idea of PM-MTGSR is that every similar patch group x_{G_k} can be approximately reconstructed by the linear combination of a few atoms from the group dictionary $D_{G_k} \in \mathbb{R}^{B\times gh}$. D_{G_k} is concatenated by h atoms of $d^i_{G_k} \in \mathbb{R}^{B\times g}$, i.e., $D_{G_k} = \left[d^1_{G_k}, d^2_{G_k}, \ldots, d^h_{G_k}\right]$. We assume that the group sparse coefficient $\alpha_{G_k} \in \mathbb{R}^{B\times Bh}$ is also concatenated by $\alpha^i_{G_k} \in \mathbb{R}^{B\times B}$ (i.e., $\alpha_{G_k} = \left[\alpha^1_{G_k}, \alpha^2_{G_k}, \ldots, \alpha^h_{G_k}\right] \in \mathbb{R}^{B\times Bh}$). Then, the PM-MTGSR for x_{G_k} (hereafter, x_{G_k} means the similar patch group after patch matching, not the original group) is

$$x_{G_k} = D_{G_k} \circ \alpha_{G_k} = \sum_{i=1}^{h} \alpha^i_{G_k} d^i_{G_k}, \quad k = 1, 2, \ldots, K \tag{18}$$

where the notation ($\circ$) represents the special atom product of the two multipliers. Then, for the missing information reconstruction, we have

$$\underset{D_{G_k}, \alpha_{G_k}}{\arg\min} \frac{1}{2} \sum_{k=1}^{K} \left\| M_{G_k} \otimes \left(x_{G_k} - D_{G_k} \circ \alpha_{G_k}\right) \right\|_2^2 + \lambda \sum_{k=1}^{K} \left\| \alpha_{G_k} \right\|_0 \tag{19}$$

with

$$M_{G_k} = p_{G_k}(M), \quad k = 1, 2, \ldots, K \tag{20}$$

where $M \in \mathbb{R}^{mnT\times 1}$ is a mask of x signifying where the information is missing, which consists of ones and zeros, with the zeros representing the missing data; similarly, $M_{G_k} \in \mathbb{R}^{B\times g}$ is the mask of x_{G_k}, ($\otimes$) represents the pointwise product of the two multipliers, λ is the regularization parameter, $\|\bullet\|_2$ is the Frobenius norm, and $\|\bullet\|_0$ is the ℓ_0 norm. In (19), the first item is the data fidelity term and the second one is the regularization term. This expression is an ill-posed joint optimization of D_{G_k} and α_{G_k}, which is usually solved by alternately optimizing D_{G_k} and α_{G_k}. First, as the K-SVD method [47] done, all the atoms of D_{G_k} can be updated. Then, on the basis of the known D_{G_k}, α_{G_k} is updated by the split Bregman method as in [37], which is estimated by hard thresholding [48] as follows:

$$\alpha_{G_k} = hard\left(\gamma_{G_k}, \sqrt{2\sigma}\right) = \gamma_{G_k} \otimes \left(|\gamma_{G_k}| > \sqrt{2\sigma}\right) \tag{21}$$

with

$$\sigma = \frac{\lambda g B K}{\tau m n T} \tag{22}$$

where γ_{G_k} is the singular values of residual error matrix in the K-SVD dictionary update process, τ is a parameter introduced in the process of split Bregman method.

Finally, x_{G_k} is reconstructed by

$$x_{G_k} = D_{G_k} \circ \alpha_{G_k} \tag{23}$$

where ($\circ$) is the same as in (18). The reconstructed target patch equates to the first column of x_{G_k}

$$x_k = x^1_{G_k}. \tag{24}$$

The complete reconstructed version of x is

$$x = \sum_{k=1}^{K} p_k^T\left(x_k\right) \odot \sum_{k=1}^{K} p_k^T\left(y_k\right) \tag{25}$$

where $p_k^T(\bullet)$ denotes the pseudoinverse operation of $p_k(\bullet)$, which puts the kth patch back to its original position in the

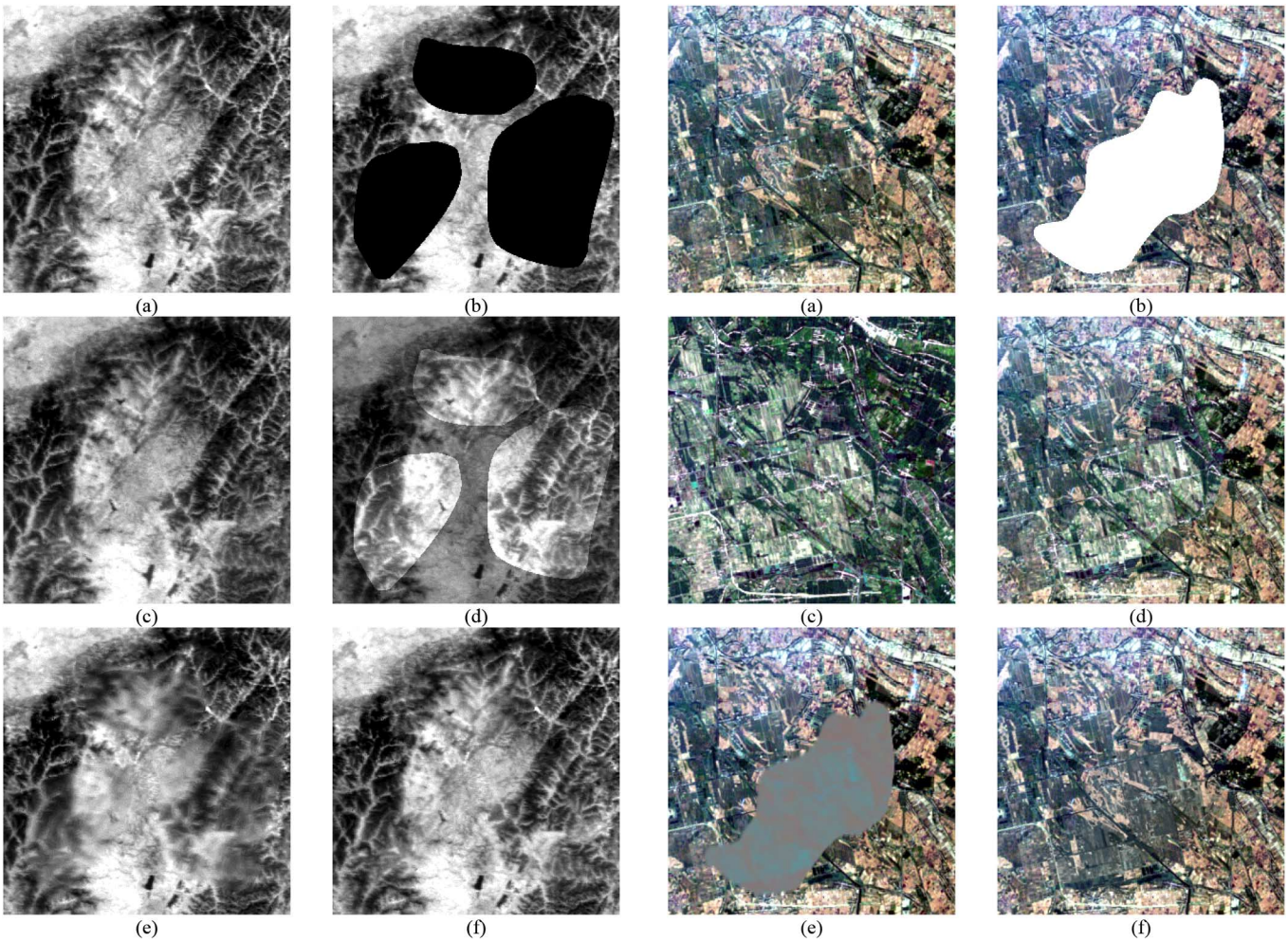

Fig. 5. Simulated reconstruction of a MODIS reflectance image using the different methods. (a) The original image. (b) Corrupted image. (c) Auxiliary image. (d) Reconstruction using direct replacement of the auxiliary image. (e) Reconstruction using MT-KSVD [32]. (f) Reconstruction using the proposed PM-MTGSR.

Fig. 6. Simulated reconstruction of a TM image using the different methods. (a) Original image. (b) Corrupted image. (c) Auxiliary image. (d) Reconstruction using direct replacement of the auxiliary image. (e) Reconstruction using MT-KSVD [32]. (f) Reconstruction using the proposed PM-MTGSR.

image, padded with zeros elsewhere, y_k is all ones with the same length as x_k, and $(\odot)$ denotes the pointwise division. Note that instead of reconstructing all the patches in x_{G_k}, we just reconstruct the target patch (the first column of x_{G_k}). In this way, to some degree, the smoothing effect can be alleviated. However, the target patches are partly overlapping, so the corresponding parts should be averaged by the number of times they are overlapped.

III. Missing Information Reconstruction Experiments

In order to qualitatively and quantitatively verify the validity of the proposed PM-MTGSR algorithm, we undertook both simulated and real-data experiments. For multitemporal data, they may change greatly or not significantly. Therefore, data representative of each category was used in the experiments. In other words, we deliberately chose stable 500-m resolution MODIS reflectance images and unstable Landsat TM images as the experimental data. For the 500-m resolution MODIS reflectance images, they have seven bands, and we only processed one band. For the TM images, three bands (red, green, and blue) were used. In general, in the experiments, one image was corrupted or cloud contaminated and the other temporal one was intact (as the auxiliary image). The value of the MODIS reflectance images ranges from 0 to 1, and the value of the TM images ranges from 1 to 255. For consistency of the parameter setting, the TM images were normalized to [0,1]. The experimental data were also georeferenced before the reconstruction was conducted. The experimental platform was a PC with an Intel 3.4-GHz CPU and 8 GB of memory. Without any special instructions, the parameters were set as follows: $\tau = 0.02$, $\lambda = 1.5 \times 10^{-4}$, $g = 20$ (for the nonadaptive approach), $r = 20$, $T = 2$, $B = 16$, $w = 2$, $m = 300$ (image size), $n = 300$ (image size), and the window size of the normalization was set to 80. The indicator threshold for Q_E, Q_{JM}, Q_{Can}, Q_{MAE}, and Q_{MRE} was 0.5×10^{-4}, and the indicator threshold for Q_{CC}, Q_{Cos}, Q_{GD}, and Q_{GJ} was 0.95. The default similarity indicator was Q_{CC}. Additionally, the adaptive approach for searching for similar patches was adopted.

A. Simulated Experiments

First, two simulated experiments were undertaken. Each experiment involved two images: one was the original image and the other was the auxiliary image. Parts of the original image were artificially removed and then reconstructed. Since the original images were available, quantitative evaluation was possible. For the MODIS reflectance images, the original and auxiliary images were acquired on March 5, 2008, and April 6, 2008, respectively. For the TM images, the original and auxiliary images were acquired on September 27, 2001 and July 22, 2001, respectively.

To demonstrate the effect of the proposed PM-MTGSR, we contrasted its reconstruction with those of direct replacement of the auxiliary image with the missing area and multitemporal K-SVD (MT-KSVD) [32]. Since the GSR approach in [37] cannot be directly applied to multitemporal remote-sensing images, we do not show its reconstruction. The corresponding results of the MODIS reflectance images and the TM true-color images are shown in Figs. 5 and 6, respectively. In terms of the stable MODIS reflectance images, Fig. 5(a) and (c) is the original and auxiliary images, respectively, and although they are stable to some degree, the direct replacement result [Fig. 5(d)] shows an obvious temporal difference. MT-KSVD [Fig. 5(e)] succeeds in reducing this kind of radiance difference; however, since the number of auxiliary images is not sufficient, the reconstruction is oversmoothed (MT-KSVD is good at the processing of multiple images). In contrast, PM-MTGSR [Fig. 5(f)] effectively reconstructs the missing information. This is because it takes the correlations between patches into consideration, rather than the independent sparse representation of every patch, as in MT-KSVD. As far as the unstable TM images are concerned, Fig. 6(a) and (c) is the original and auxiliary images, respectively, based on the direct replacement in Fig. 6(d), and we can see that their ground features vary greatly. In this situation, as shown in Fig. 6(e), MT-KSVD cannot reconstruct the significant temporal difference, and the effect is very poor. Fortunately, PM-MTGSR [Fig. 6(f)] reconstructs a satisfactory result, which is basically consistent with the original image. This indicates that when the temporal difference is great, patch correlation is meaningful. Generally speaking, for both the stable MODIS reflectance images and the unstable TM images, the proposed PM-MTGSR can successfully reconstruct the missing information and performs better than MT-KSVD, which is because the nonlocal similarity between patches benefits the missing information reconstruction.

In order to further distinguish the reconstruction effects, scatter plots between the reconstructed region and the original region are shown in Figs. 7 and 8. Fig. 7(a)–(c) is for Fig. 5(d)–(f), and 8(a)–(c) are for Fig. 6(d)–(f). For the reconstruction of the MODIS reflectance image, the points on the scatter plot of direct replacement [shown in Fig. 7(a)] deviate from the red diagonal and are worse than for MT-KSVD and PM-MTGSR. Additionally, the points on the scatter plots of PM-MTGSR show a more compact distribution than those of MT-KSVD, but the advantage is not obvious. This is because the temporal difference is small, and the patch matching of PM-MTGSR cannot significantly enhance the correlations between

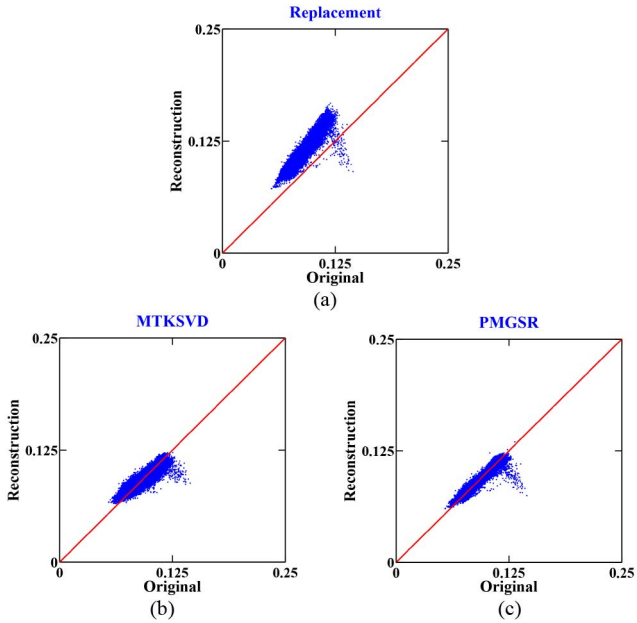

Fig. 7. Scatter plots between the original and reconstructed pixels (only for the missing areas) in Fig. 5. (a) Direct replacement in Fig. 5(d). (b) MT-KSVD in Fig. 5(e). (c) PM-MTGSR in Fig. 5(f).

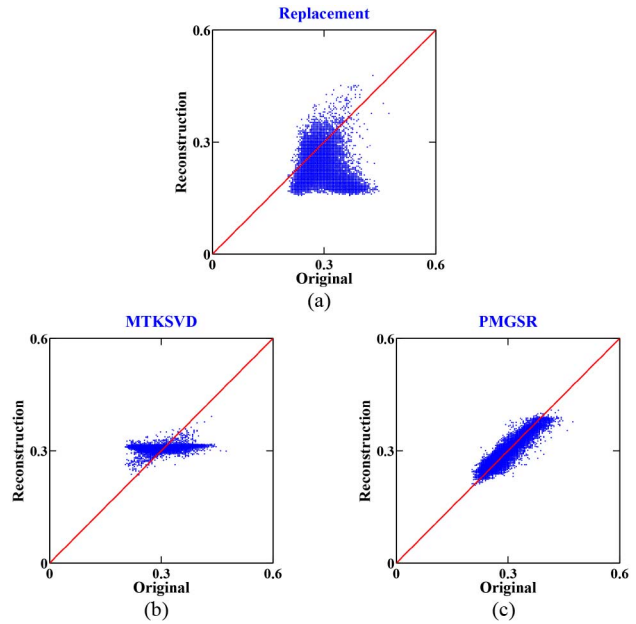

Fig. 8. Scatter plots between the original and reconstructed pixels (only for the missing areas) in Fig. 6. (a) Direct replacement in Fig. 6(d). (b) MT-KSVD in Fig. 6(e). (c) PM-MTGSR in Fig. 6(f).

the target patch and similar patches. As for the scatter plots of the TM image in Fig. 8, the scatter plots of direct replacement and MT-KSVD are again worse than that of PM-MTGSR. The difference with Fig. 7 is that the scatter plot of PM-MTGSR is obviously better than that of MT-KSVD. Benefitting from the patch matching, the difference between the target patch and similar patches is markedly weakened. As a result, PM-MTGSR obtains a better reconstruction than MT-KSVD. In summary, according to the scatter plots, PM-MTGSR obtains a

TABLE I
QUANTITATIVE EVALUATION OF THE RECOVERY RESULTS OF THE DIFFERENT METHODS (PART I)

Images	Methods	MAE/10^{-3}	MSE/10^{-5}	MRE/%	CC	Time/min
Fig. 5	Corrupted	94.4501	908.7120	100.0000	–	–
	Replacement	24.1471	62.5120	25.5851	0.9347	–
	MT-KSVD	4.3201	3.2120	4.6458	0.9018	6.0958
	PM-MTGSR	**2.6531**	**1.5120**	**2.8314**	**0.9548**	**2.9417**
Fig. 6	Corrupted	321.3051	10544.6120	100.0000	–	–
	Replacement	43.3421	346.1120	13.2046	0.5684	–
	MT-KSVD	21.7451	80.2120	7.3239	0.8338	20.3646
	PM-MTGSR	**8.3961**	**12.8120**	**2.7440**	**0.9712**	**8.7947**

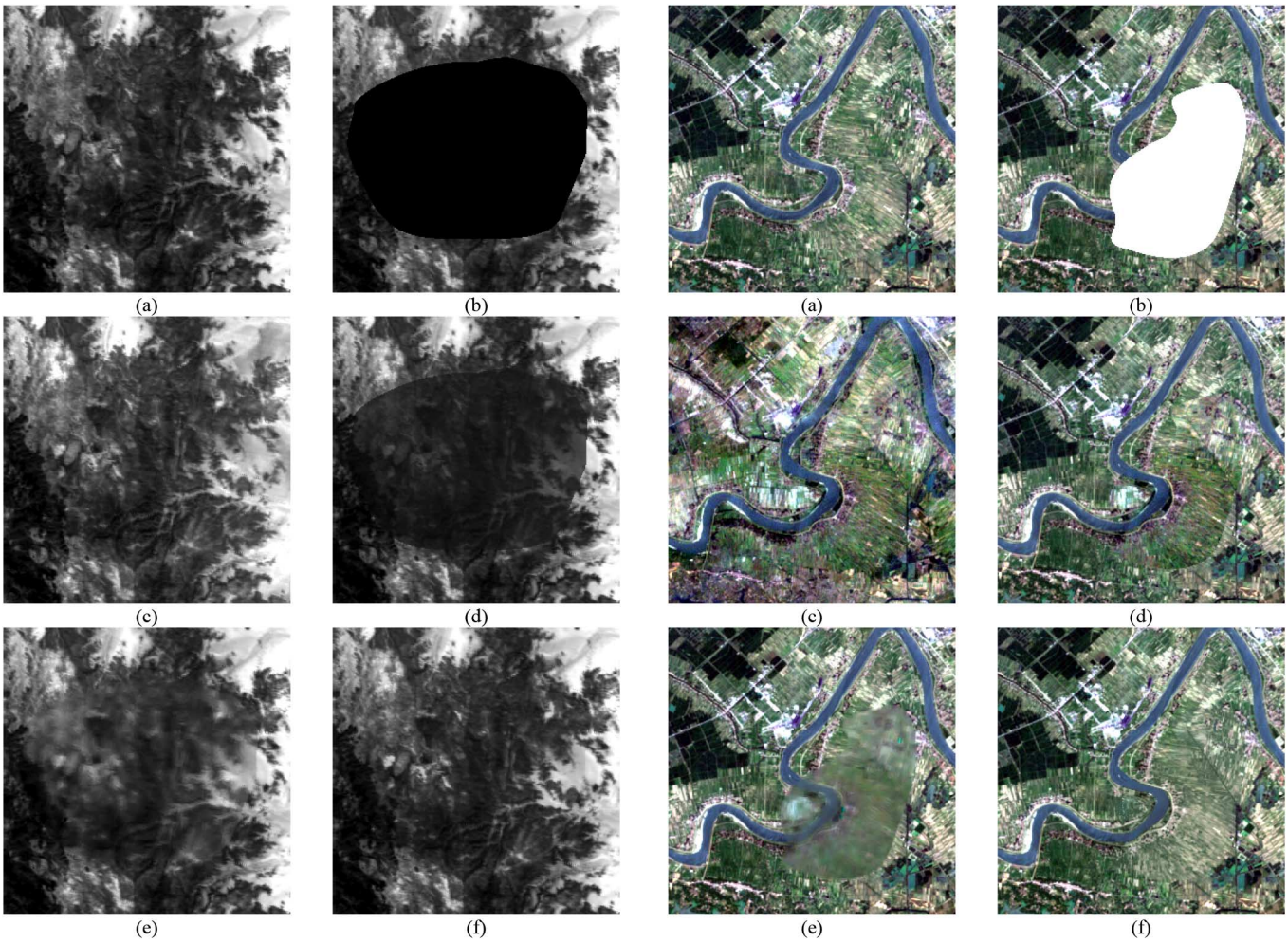

Fig. 9. Simulated reconstruction of a MODIS reflectance image using the different methods. (a) Original image. (b) Corrupted image. (c) Auxiliary image. (d) Reconstruction using direct replacement of the auxiliary image. (e) Reconstruction using MT-KSVD [32]. (f) Reconstruction using the proposed PM-MTGSR.

Fig. 10. Simulated reconstruction of a TM image using the different methods. (a) Original image. (b) Corrupted image. (c) Auxiliary image. (d) Reconstruction using direct replacement of the auxiliary image. (e) Reconstruction using MT-KSVD [32]. (f) Reconstruction using the proposed PM-MTGSR.

better reconstruction result than MT-KSVD. When the temporal difference is obvious, the advantage is greater.

After the previous qualitative comparison, we now focus on a quantitative comparison of the different methods. The evaluation indicators are MAE, MRE, CC, and mean-squared error (MSE). MAE, MRE, and CC are calculated by (7)–(9), respectively. MSE has the same meaning as (4). For MAE, MSE, and MRE, the lower the value, the better the result. For CC, the higher the value, the better the result. The quantitative evaluation is shown in Table I. For both the MODIS reflectance image and the TM image, compared to the corrupted image itself, all three methods can improve the quantitative indicators, which mean an effective reconstruction. However, direct replacement using another temporal image cannot achieve a

TABLE II
QUANTITATIVE EVALUATION OF THE RECOVERY RESULTS OF THE DIFFERENT METHODS (PART II)

Images	Methods	MAE/10^{-3}	MSE/10^{-5}	MRE/%	CC	Time/min
Fig. 9	Corrupted	126.8371	1683.7120	100.0000	–	–
	Replacement	18.6731	60.6120	13.0716	0.9529	–
	MT-KSVD	8.4651	12.3120	6.7903	0.9148	8.6023
	PM-MTGSR	**4.7221**	**4.1120**	**3.6454**	**0.9734**	**4.3312**
Fig. 10	Corrupted	295.3541	8916.8120	100.0000	–	–
	Replacement	82.4111	790.0120	29.4818	0.6610	–
	MT-KSVD	26.0001	131.0120	8.8973	0.6642	21.6219
	PM-MTGSR	**10.5791**	**22.3120**	**3.7334**	**0.9409**	**8.5065**

satisfactory reconstruction. Since it completely ignores the temporal variation, its evaluation is the worst among all three methods. MT-KSVD obtains a better result than direct replacement because it makes use of the sparse property of the remote-sensing data, i.e., to some extent, it can capture the temporal variation. Even though MT-KSVD is based on the latent sparsity of the patch-based remote-sensing data, it ignores the relationship or similarity between patches. As a result, MT-KSVD does not perform better than PM-MTGSR, which takes the patch similarity into consideration. However, GSR and PM-MTGSR work differently when they utilize the patch similarity. GSR first searches for the similar patches to the target patch and then groups them for the sparse representation. In contrast, PM-MTGSR carries out patch matching after the similar patches are found. With the help of the patch matching, the similarities between the target patch and the similar patches are strengthened. PM-MTGSR therefore obtains the best result. From the perspective of operating efficiency, thanks to the split Bregman acceleration strategy, PM-MTGSR outperforms MT-KSVD. Additionally, PM-MTGSR directly reconstructs the target patch, rather than the similar group like GSR, so the time is shortened further. Overall, a ranking of the reconstruction effects from worst to best is as follows: direct replacement, MT-KSVD, and PM-MTGSR.

To ensure a comprehensive assessment of the proposed algorithm, we also conducted another two similar simulated experiments. For the MODIS reflectance images, the original and auxiliary images were acquired on November 2, 2013, and November 4, 2013, respectively. For the TM images, the original and auxiliary images were acquired on July 22, 2001, and May 3, 2001, respectively. The corresponding reconstruction results are shown in Figs. 9 and 10, respectively. The quantitative evaluation is shown in Table II. The two extra experiments allowed the same conclusion as the previous experiments and again showed that the proposed PM-MTGSR is very effective.

We now investigate several factors which influence PM-MTGSR itself. The first factor is the similarity indicators used in the search for similar patches. In the experiments, the data consisted of Figs. 5 and 6 and the listed indicators in Section III-B. To ensure the reliability, all the parameters except for the similarity indicator were identical. Table III shows the quantitative assessment of the reconstruction results of the different similarity indicators. As shown in the table, for both the MODIS reflectance image and the TM image, all the indicators successfully reconstruct the missing information. Moreover, the differences in the reconstructions are very small. Although different similarity indicators may select different patches to form a group, the patch matching reduces their differences. Therefore, the differences in the reconstruction results are small. On the whole, CC as the similarity indicator performs a little better than the other indicators. This experiment demonstrates that PM-MTGSR is relatively robust with regard to different similarity indicators.

TABLE III
QUANTITATIVE EVALUATION OF THE PROPOSED PM-MTGSR USING DIFFERENT SIMILARITY INDICATORS

Images	Indicators	MAE/10^{-3}	MSE/10^{-5}	MRE/%	CC	Time/min
Fig. 5	Q_E	2.7581	1.6120	2.9434	0.9520	2.4623
	Q_{JM}	2.7511	1.6120	2.9364	0.9521	2.6159
	Q_{Can}	2.7631	1.6120	2.9496	0.9518	2.7184
	Q_{MAE}	2.7621	1.6120	2.9494	0.9519	2.2390
	Q_{MRE}	2.7621	1.7120	2.9467	0.9495	2.5626
	Q_{CC}	**2.6531**	**1.5120**	**2.8314**	**0.9548**	**2.9417**
	Q_{Cos}	2.6991	1.5120	2.8816	0.9540	2.6216
	Q_{GD}	2.7711	1.6120	2.9578	0.9523	2.6182
	Q_{GM}	2.7701	1.6120	2.9486	0.9517	2.5236
Fig. 6	Q_E	8.4611	13.1120	2.7601	0.9705	6.6841
	Q_{JM}	8.4611	13.1120	2.7602	0.9705	7.9496
	Q_{Can}	8.4831	13.1120	2.7671	0.9704	8.0061
	Q_{MAE}	8.4831	13.2120	2.7669	0.9703	6.7937
	Q_{MRE}	9.0361	14.4120	2.9506	0.9679	7.7695
	Q_{CC}	**8.3961**	**12.8120**	**2.7440**	**0.9712**	**8.7947**
	Q_{Cos}	8.4061	12.9120	2.7447	0.9710	7.8650
	Q_{GD}	8.5131	13.3120	2.7729	0.9699	7.7532
	Q_{GM}	8.5131	13.3120	2.7729	0.9699	7.5932

We now discuss how the number of similar patches affects the reconstruction effect. A series of reconstruction experiments for Figs. 5 and 6 were conducted. For these experiments, the number of similar patches was varied. Fig. 11 shows the CC variation diagrams with the number of similar patches. The CC is calculated from the original and reconstructed pixels. As shown in Fig. 11(a) and (b), for both the MODIS reflectance image and the TM image, the CC gradually decreases as the number of similar patches increases. This is because the newly added similar patches are less similar to the target patch and bring more harmful noise. However, the decrease is very small. When the number of similar patches increases from 10 to 80,

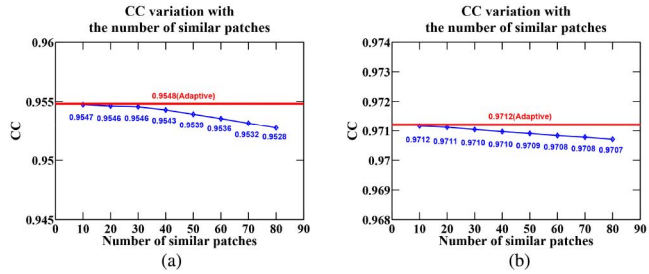

Fig. 11. CC variation with the number of similar patches. (a) MODIS reflectance image in Fig. 5. (b) TM image in Fig. 6.

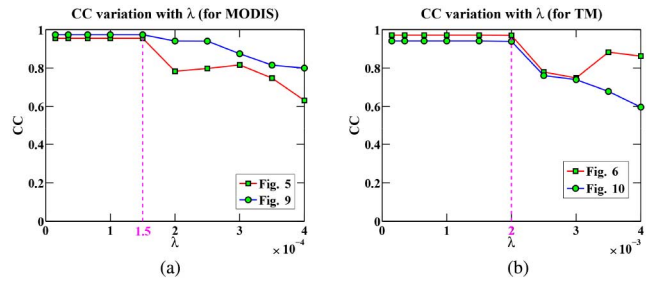

Fig. 12. CC variation with λ. (a) MODIS reflectance images in Figs. 5 and 9. (b) TM images in Figs. 6 and 10.

the CC only decreases by 0.03% and 0.05%, respectively. In other words, the proposed PM-MTGSR is relatively robust with regard to the number of similar patches. In addition, the red lines in the two subfigures represent the CC using adaptive search, and it can be seen that the adaptive method is a little better than a fixed number of similar patches. It is also worth noting that the adaptive method takes less time than the fixed number approach. Overall, the number of similar patches has a limited influence on the reconstruction result.

In order to explore the influence of the regularization parameter λ in (22) on the reconstruction, a series of reconstruction experiments for the MODIS reflectance images and the TM images with different values of λ were conducted. When λ was varied, the other parameter τ was fixed as 0.02 (we discuss parameter τ in the next part). The CCs of the reconstruction results are shown in Fig. 12. Fig. 12(a) is for the MODIS reflectance images, and Fig. 12(b) is for the TM images. As shown in these two subfigures, when the value of λ is small, the reconstruction result is satisfactory, and this trend remains unchanged within a certain range; however, when λ is a large value, the reconstruction result is very poor. These experimental results demonstrate that a suitable value of λ is of great significance for the reconstruction. Although the optimal λ is different for the MODIS reflectance images and the TM images, as shown in Fig. 12, both MODIS images share the same optimal value of λ, as do the TM images. As a result, we can easily obtain the optimal value of λ via simulated experiments and then apply it to real-data experiments. These experiments demonstrate that λ is very important for the reconstruction of PM-MTGSR, and the optimal value of λ is usually the same for the same kind of remote-sensing image.

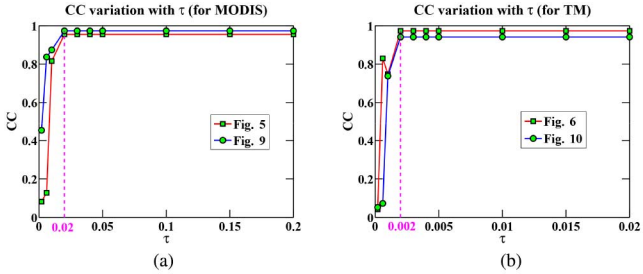

Fig. 13. CC variation with τ. (a) MODIS reflectance images in Figs. 5 and 9. (b) TM images in Figs. 6 and 10.

TABLE IV
QUANTITATIVE EVALUATION OF THE RECOVERY RESULTS USING DIFFERENT SIZES OF NORMALIZATION WINDOW

Images	Size	MAE/10^{-3}	MSE/10^{-5}	MRE/%	CC	Time /min
Fig. 5	20	3.0361	1.8120	3.2700	0.9434	3.8620
	40	2.7581	1.6120	2.9531	0.9517	3.1866
	60	2.6631	1.5120	2.8443	0.9550	3.0404
	80	**2.6531**	**1.5120**	**2.8314**	**0.9548**	**2.9417**
	100	2.6911	1.5120	2.8736	0.9538	3.0011
Fig. 6	20	9.3241	14.7120	3.0437	0.9692	9.3651
	40	9.0021	14.0120	2.9386	0.9697	10.2477
	60	8.7401	13.6120	2.8581	0.9701	9.4018
	80	**8.3961**	**12.8120**	**2.7440**	**0.9712**	**8.7947**
	100	8.3211	12.8120	2.7147	0.9710	9.2272

In the same way as we tested regularization parameter λ, we also investigated the effect of the other regularization parameter τ in (22). When τ was varied, λ was fixed as 1.5×10^{-4}. The CCs of the reconstruction results are shown in Fig. 13. Fig. 13(a) is for the MODIS reflectance images, and Fig. 13(b) is for the TM images. For both the MODIS and TM images, the variation trend of CC with τ is consistent: it first rises and then remains steady. As can be clearly seen, τ also has a great impact on the reconstruction. An optimal value of τ is therefore necessary for a satisfactory reconstruction. As with parameter λ, both MODIS images share the same optimal value, and the TM images also share the same optimal value. Via simulated experiments, the optimal value of τ for a certain kind of remote-sensing image can be easily determined. These experiments show that parameter τ is also important for the reconstruction of PM-MTGSR, and the optimal value of τ is usually the same for the same kind of remote-sensing image.

In Section II-A, we noted that the normalization is undertaken within a local window. Accordingly, we now analyze how the size of normalization window influences the reconstruction result. Based on the MODIS reflectance image and the TM image in Figs. 5 and 6, respectively, we undertook a sequence of reconstruction experiments with different sizes of normalization window. The quantitative evaluation results are shown in Table IV. As can be seen in Table IV, as the size of window increases, the result first increases to the optimal level and then declines. For the two images, a local window size of 80 is the best size.

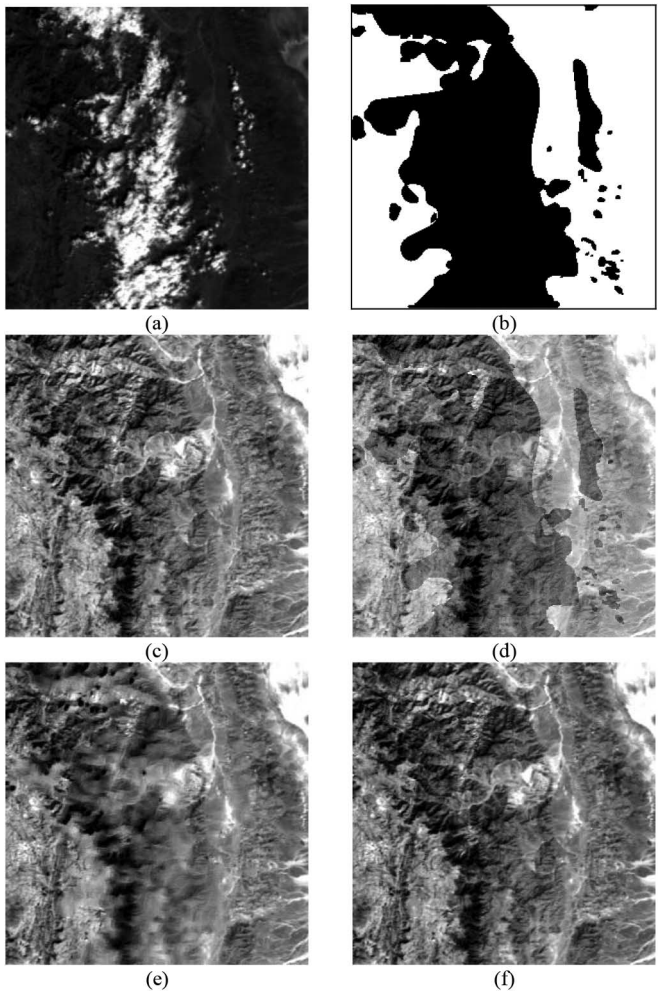

Fig. 14. Real-data reconstruction of a MODIS image using the different methods. (a) Original image. (b) Cloud mask. (c) Auxiliary image. (d) Reconstruction using direct replacement of the auxiliary image. (e) Reconstruction using MT-KSVD [32]. (f) Reconstruction using the proposed PM-MTGSR.

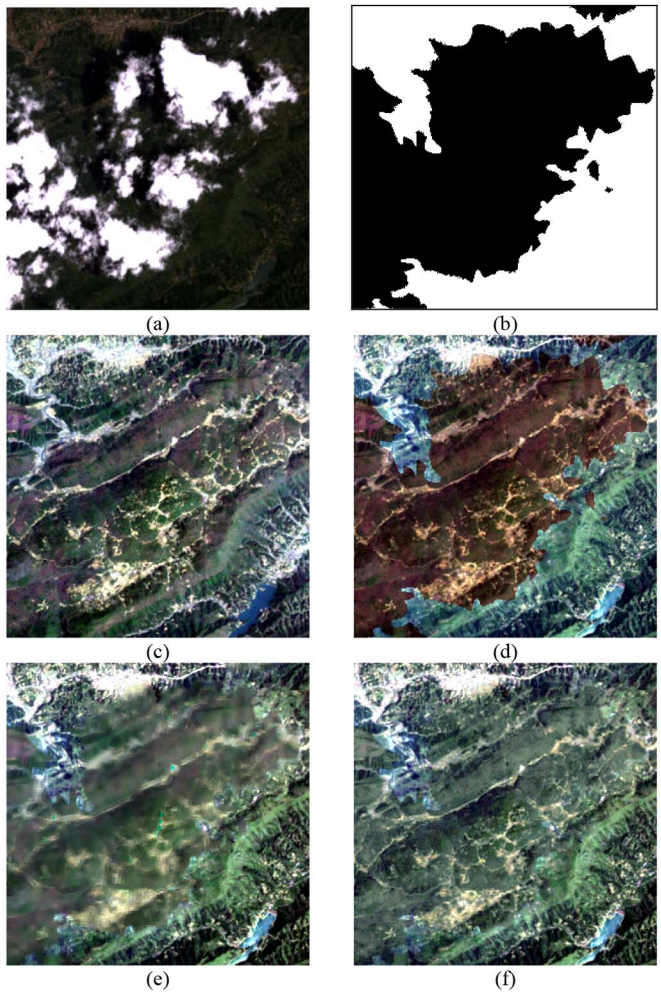

Fig. 15. Real-data reconstruction of a TM image using the different methods. (a) Original image. (b) Cloud mask. (c) Auxiliary image. (d) Reconstruction using direct replacement of the auxiliary image. (e) Reconstruction using MT-KSVD [32]. (f) Reconstruction using the proposed PM-MTGSR.

B. Real-Data Experiments

After the simulated experiments, real-data experiments were also undertaken. Similarly, the experimental data consisted of MODIS reflectance images and TM images. For the MODIS reflectance images, the cloud-contaminated and auxiliary images were acquired on December 2 and 11, 2008, respectively. For the TM images, the cloud-contaminated and auxiliary images were acquired on July 22, 2001 and May 3, 2001, respectively. As cloud detection was not our focus in this work, the cloud masks were manually drawn. The corresponding reconstruction results are shown in Figs. 14 and 15. For both the stable MODIS reflectance image and the unstable TM image, the reconstruction results [Figs. 14(d) and 15(d)] using direct replacement show inconsistent transitions at the cloud edges. This is because the temporal difference is inherited from the auxiliary image. MT-KSVD [Figs. 14(e) and 15(e)] obtains a better reconstruction result in this sense. However, because of the absence of sufficient auxiliary images, the MT-KSVD result is still oversmoothed, as in the simulated experiments. In contrast, the PM-MTGSR results [Figs. 14(f) and 15(f)] show a more natural visual effect. The real-data experiments also confirm that the proposed PM-MTGSR is very effective.

IV. Conclusion

In this paper, we have proposed the PM-MTGSR method for the reconstruction of the missing information of optical remote-sensing data. PM-MTGSR is suitable for cases of sensor failure (e.g., Aqua MODIS band 6) and thick cloud cover. Since the reconstruction of data affected by cloud cover is more challenging, we focused on this aspect in our experiments. A target image (to be reconstructed) and auxiliary image(s) are needed for PM-MTGSR. First, the auxiliary image is normalized to the target image so that the differences are weakened. The auxiliary and target images are then reordered by IIL to two dimensions and divided into a series of partly overlapping patches. On this basis, the similar patches are found and then grouped for the joint sparse representation. In the process, the similar patches are matched with the target patch to be reconstructed. Since the similarity between the patches is considered and strengthened,

the reconstruction effect is satisfactory. Through both simulated and real-data experiments, the proposed PM-MTGSR was demonstrated to be more effective than the state-of-the-art MT-KSVD. Although the experiments only considered two images from different times, the method is also suitable for use with more than two images, and the corresponding reconstruction should be better. In this work, automatic cloud detection was not considered, which will be a very interesting research topic in our future work.

REFERENCES

[1] H. Shen, X. Li, L. Zhang, D. Tao, and C. Zeng, "Compressed sensing based inpainting of aqua moderate resolution imaging spectroradiometer band 6 using adaptive spectrum-weighted sparse Bayesian dictionary learning," *IEEE Trans. Geosci. Remote Sens.*, vol. 52, no. 2, pp. 894–906, Feb. 2014.

[2] C. Zeng, H. Shen, and L. Zhang, "Recovering missing pixels for Landsat ETM+ SLC-off imagery using multi-temporal regression analysis and a regularization method," *Remote Sens. Environ.*, vol. 131, pp. 182–194, Apr. 2013.

[3] C.-H. Lin, K.-H. Lai, Z.-B. Chen, and J.-Y. Chen, "Patch-based information reconstruction of cloud-contaminated multitemporal images," *IEEE Trans. Geosci. Remote Sens.*, vol. 52, no. 1, pp. 163–174, Jan. 2014.

[4] C. Zhang, W. Li, and D. Travis, "Gaps-fill of SLC-off Landsat ETM+ satellite image using a geostatistical approach," *Int. J. Remote Sens.*, vol. 28, no. 22, pp. 5103–5122, 2007.

[5] A. Maalouf, P. Carre, B. Augereau, and C. Fernandez-Maloigne, "A bandelet-based inpainting technique for clouds removal from remotely sensed images," *IEEE Trans. Geosci. Remote Sens.*, vol. 47, no. 7, pp. 2363–2371, Jul. 2009.

[6] M. Bertalmio, G. Sapiro, V. Caselles, and C. Ballester, "Image inpainting," in *Proc. 27th Annu. Conf. Comput. Graph. Interactive Techn. (SIGGRAPH'00)*, New Orleans, LA, USA, 2000, pp. 417–424.

[7] H. Shen and L. Zhang, "A MAP-based algorithm for destriping and inpainting of remotely sensed images," *IEEE Trans. Geosci. Remote Sens.*, vol. 47, no. 5, pp. 1492–1502, May 2009.

[8] Q. Cheng, H. Shen, L. Zhang, and P. Li, "Inpainting for remotely sensed images with a multichannel nonlocal total variation model," *IEEE Trans. Geosci. Remote Sens.*, vol. 52, no. 1, pp. 175–187, Jan. 2014.

[9] A. Criminisi, P. Perez, and K. Toyama, "Region filling and object removal by exemplar-based image inpainting," *IEEE Trans. Image Process.*, vol. 13, no. 9, pp. 1200–1212, Sep. 2004.

[10] P. Rakwatin, W. Takeuchi, and Y. Yasuoka, "Restoration of Aqua MODIS Band 6 using histogram matching and local least squares fitting," *IEEE Trans. Geosci. Remote Sens.*, vol. 47, no. 2, pp. 613–627, Feb. 2009.

[11] H. Shen, C. Zeng, and L. Zhang, "Recovering reflectance of AQUA MODIS band 6 based on within-class local fitting," *IEEE J. Sel. Topics Appl. Earth Observ. Remote Sens.*, vol. 4, no. 1, pp. 185–192, Mar. 2011.

[12] I. Gladkova, M. D. Grossberg, F. Shahriar, G. Bonev, and P. Romanov, "Quantitative restoration for MODIS band 6 on aqua," *IEEE Trans. Geosci. Remote Sens.*, vol. 50, no. 6, pp. 2409–2416, Jun. 2012.

[13] X. Li, H. Shen, L. Zhang, H. Zhang, and Q. Yuan, "Dead pixel completion of aqua MODIS band 6 using a robust M-estimator multiregression," *IEEE Geosci. Remote Sens. Lett.*, vol. 11, no. 4, pp. 768–772, Apr. 2014.

[14] Z. Wang, J. Jin, J. Liang, K. Yan, and Q. Peng, "A new cloud removal algorithm for multi-spectral images," in *Proc. 4th Int. Symp. Multispectral Image Process. Pattern Recognit. (MIPPR'05)*, Wuhan, China, 2005, vol. 6043, pp. 60430W-1–60430W-11.

[15] C. Feng, J.-W. Ma, Q. Dai, and X. Chen, "An improved method for cloud removal in ASTER data change detection," in *Proc. IEEE Int. Geosci. Remote Sens. Symp. (IGARSS'04)*, Anchorage, AK, USA, 2004, pp. 3387–3389.

[16] H. Li, L. Zhang, and H. Shen, "A variational gradient-based fusion method for visible and SWIR imagery," *Photogramm. Eng. Remote Sens.*, vol. 78, no. 9, pp. 947–958, Sep. 2012.

[17] D.-C. Tseng, H.-T. Tseng, and C.-L. Chien, "Automatic cloud removal from multi-temporal SPOT images," *Appl. Math. Comput.*, vol. 205, no. 2, pp. 584–600, Nov. 2008.

[18] B. N. Holben, "Characteristics of maximum-value composite images from temporal AVHRR data," *Int. J. Remote Sens.*, vol. 7, no. 11, pp. 1417–1434, 1986.

[19] C.-H. Lin, P.-H. Tsai, K.-H. Lai, and J.-Y. Chen, "Cloud removal from multitemporal satellite images using information cloning," *IEEE Trans. Geosci. Remote Sens.*, vol. 51, no. 1, pp. 232–241, Jan. 2013.

[20] F. Melgani, "Contextual reconstruction of cloud-contaminated multitemporal multispectral images," *IEEE Trans. Geosci. Remote Sens.*, vol. 44, no. 2, pp. 442–455, Feb. 2006.

[21] M. Li, S. C. Liew, and L. K. Kwoh, "Producing cloud free and cloud-shadow free mosaic from cloudy IKONOS images," in *Proc. IEEE Int. Geosci. Remote Sens. Symp. (IGARSS'03)*, Toulouse, France, 2003, pp. 3946–3948.

[22] E. Helmer and B. Ruefenacht, "Cloud-free satellite image mosaics with regression trees and histogram matching," *Photogramm. Eng. Remote Sens.*, vol. 71, no. 9, pp. 1079–1089, Sep. 2005.

[23] E. Addink, "A comparison of conventional and geostatistical methods to replace clouded pixels in NOAA-AVHRR images," *Int. J. Remote Sens.*, vol. 20, no. 5, pp. 961–977, 1999.

[24] C. Zhang, W. Li, and D. J. Travis, "Restoration of clouded pixels in multispectral remotely sensed imagery with cokriging," *Int. J. Remote Sens.*, vol. 30, no. 9, pp. 2173–2195, 2009.

[25] M. J. Pringle, M. Schmidt, and J. S. Muir, "Geostatistical interpolation of SLC-off Landsat ETM+ images," *ISPRS J. Photogramm. Remote Sens.*, vol. 64, no. 6, pp. 654–664, Nov. 2009.

[26] N. Viovy, O. Arino, and A. S. Belward, "The best index slope extraction (BISE): A method for reducing noise in NDVI time-series," *Int. J. Remote Sens.*, vol. 13, no. 8, pp. 1585–1590, 1992.

[27] A. Savitzky and M. J. E. Golay, "Smoothing and differentiation of data by simplified least squares procedures," *Anal. Chem.*, vol. 36, no. 8, pp. 1627–1639, Jul. 1964.

[28] P. Jönsson and L. Eklundh, "Seasonality extraction by function fitting to time-series of satellite sensor data," *IEEE Trans. Geosci. Remote Sens.*, vol. 40, no. 8, pp. 1824–1832, Aug. 2002.

[29] P. S. Beck, C. Atzberger, K. A. Høgda, B. Johansen, and A. K. Skidmore, "Improved monitoring of vegetation dynamics at very high latitudes: A new method using MODIS NDVI," *Remote Sens. Environ.*, vol. 100, no. 3, pp. 321–334, Feb. 2006.

[30] W. Verhoef, M. Menenti, and S. Azzali, "Cover A colour composite of NOAA-AVHRR-NDVI based on time series analysis (1981–1992)," *Int. J. Remote Sens.*, vol. 17, no. 2, pp. 231–235, 1996.

[31] L. Lorenzi, F. Melgani, and G. Mercier, "Missing-area reconstruction in multispectral images under a compressive sensing perspective," *IEEE Trans. Geosci. Remote Sens.*, vol. 51, no. 7, pp. 3998–4008, Jul. 2013.

[32] X. Li, H. Shen, L. Zhang, H. Zhang, Q. Yuan, and G. Yang, "Recovering quantitative remote sensing products contaminated by thick clouds and shadows using multitemporal dictionary learning," *IEEE Trans. Geosci. Remote Sens.*, vol. 52, no. 11, pp. 7086–7098, Nov. 2014.

[33] X. Li, H. Shen, L. Zhang, and H. Li, "Sparse-based reconstruction of missing information in remote sensing images from spectral/temporal complementary information," *ISPRS J. Photogramm. Remote Sens.*, vol. 106, pp. 1–15, Aug. 2015.

[34] H. Shen, X. Li, Q. Cheng, C. Zeng, G. Yang, H. Li, and L. Zhang, "Missing information reconstruction of remote sensing data: A technical review," *IEEE Geosci. Remote Sens. Mag.*, vol. 3, no. 3, pp. 61–85, Sep. 2015.

[35] S. Benabdelkader and F. Melgani, "Contextual spatiospectral postreconstruction of cloud-contaminated images," *IEEE Geosci. Remote Sens. Lett.*, vol. 5, no. 2, pp. 204–208, Apr. 2008.

[36] Q. Cheng, H. Shen, L. Zhang, Q. Yuan, and C. Zeng, "Cloud removal for remotely sensed images by similar pixel replacement guided with a spatio-temporal MRF model," *ISPRS J. Photogramm. Remote Sens.*, vol. 92, pp. 54–68, Jun. 2014.

[37] J. Zhang, D. Zhao, and W. Gao, "Group-based sparse representation for image restoration," *IEEE Trans. Image Process.*, vol. 23, no. 8, pp. 3336–3351, Aug. 2014.

[38] Y. Sun, Q. Liu, J. Tang, and D. Tao, "Learning discriminative dictionary for group sparse representation," *IEEE Trans. Image Process.*, vol. 23, no. 9, pp. 3816–3828, Sep. 2014.

[39] M. Cheng, C. Wang, and J. Li, "Single-image super-resolution in RGB space via group sparse representation," *IET Image Process.*, vol. 9, no. 6, pp. 461–467, Jun. 2015.

[40] W. Gan, H. Shen, L. Zhang, and W. Gong, "Normalization of medium-resolution NDVI by the use of coarser reference data: Method and evaluation," *Int. J. Remote Sens.*, vol. 35, no. 21, pp. 7400–7429, Nov. 2014.

[41] L. Bruzzone, F. Roli, and S. B. Serpico, "An extension of the Jeffreys-Matusita distance to multiclass cases for feature selection," *IEEE Trans. Geosci. Remote Sens.*, vol. 33, no. 6, pp. 1318–1321, Nov. 1995.

[42] G. N. Lance and W. T. Williams, "Computer programs for hierarchical polythetic classification (similarity analyses)," *Comput. J.*, vol. 9, no. 1, pp. 60–64, 1966.
[43] B. Wang, X. Yan, Q. Jiang, and Z. Lv, "Generalized dice's coefficient-based multi-block principal component analysis with Bayesian inference for plant-wide process monitoring," *J. Chemom.*, vol. 29, no. 3, pp. 165–178, Mar. 2015.
[44] G.-D. Garaiman and D.-D. Garaiman, "Methods of establishing the similarity in searching by content in multimedia database with medical images," *Current Health Sci. J.*, vol. 38, no. 3, pp. 97–100, Jul. 2012.
[45] S. Li, H. Yin, and L. Fang, "Group-sparse representation with dictionary learning for medical image denoising and fusion," *IEEE Trans. Biomed. Eng.*, vol. 59, no. 12, pp. 3450–3459, Dec. 2012.
[46] D. Xu, Y. Huang, Z. Zeng, and X. Xu, "Human gait recognition using patch distribution feature and locality-constrained group sparse representation," *IEEE Trans. Image Process.*, vol. 21, no. 1, pp. 316–326, Jan. 2012.
[47] M. Aharon, M. Elad, and A. Bruckstein, "K-SVD: An algorithm for designing overcomplete dictionaries for sparse representation," *IEEE Trans. Signal Process.*, vol. 54, no. 11, pp. 4311–4322, Nov. 2006.
[48] T. Blumensath and M. E. Davies, "Iterative hard thresholding for compressed sensing," *Appl. Comput. Harmon. Anal.*, vol. 27, no. 3, pp. 265–274, Nov. 2009.

Xinghua Li (S'14) received the B.S. degree in geographical information system from Wuhan University, Wuhan, China, in 2011. He is currently pursuing the Ph.D. degree from the School of Resource and Environmental Sciences, Wuhan University.

His research interests include missing information reconstruction of remote-sensing image, cloud removal of remote-sensing image, compressed sensing-based image processing, and sparse representation.

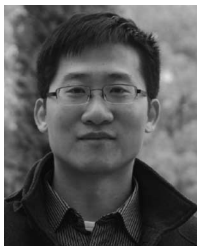

Huanfeng Shen (M'11–SM'13) received the B.S. degree in surveying and mapping engineering and the Ph.D. degree in photogrammetry and remote sensing from Wuhan University, Wuhan, China, in 2002 and 2007, respectively.

In July 2007, he joined the School of Resource and Environmental Sciences, Wuhan University, where he is currently a Luojia Distinguished Professor. He has been supported by several talent programs, such as The Youth Talent Support Program of China (2015), China National Science Fund for Excellent Young Scholars (2014), and the New Century Excellent Talents by the Ministry of Education of China (2011). He has authored or coauthored more than 100 research papers. His research interests include image quality improvement, remote-sensing mapping and application, data fusion and assimilation, and regional and global environmental change.

Dr. Shen is currently a Member of the Editorial Board of the *Journal of Applied Remote Sensing*.

Huifang Li (M'14) received the B.S. degree in geographical information science from China University of Mining and Technology, Xuzhou, China, in 2008, and the Ph.D. degree in photogrammetry and remote sensing from Wuhan University, Wuhan, China, in 2013.

She is currently working with the School of Resource and Environmental Sciences, Wuhan University, as a Lecturer. Her research interests include variational methods, dehazing, and deshadowing of remote-sensing images.

Liangpei Zhang (M'06–SM'08) received the B.S. degree in physics from Hunan Normal University, ChangSha, China, in 1982, the M.S. degree in optics from the Xi'an Institute of Optics and Precision Mechanics of Chinese Academy of Sciences, Xi'an, China, in 1988, and the Ph.D. degree in photogrammetry and remote sensing from Wuhan University, Wuhan, China, in 1998.

He is currently the Head of the Remote Sensing Division, State Key Laboratory of Information Engineering in Surveying, Mapping, and Remote Sensing (LIESMARS), Wuhan University. He is also a Chang-Jiang Scholar Chair Professor appointed by the Ministry of Education of China. He is currently a Principal Scientist for the China State Key Basic Research Project (2011–2016) appointed by the Ministry of National Science and Technology of China to lead the remote-sensing program in China. He has authored or coauthored more than 450 research papers and five books. He is the holder of 15 patents. His research interests include hyperspectral remote sensing, high-resolution remote sensing, image processing, and artificial intelligence.

Dr. Zhang is a Fellow of the Institution of Engineering and Technology (IET), an Executive Member (Board of Governor) of the China National Committee of International Geosphere–Biosphere Programme, an Executive Member of the China Society of Image and Graphics, etc. He was the General Chair of the 4th IEEE GRSS Workshop on Hyperspectral Image and Signal Processing: Evolution in Remote Sensing (WHISPERS) and the Guest Editor of JSTARS. He regularly serves as a Cochair of the series SPIE Conferences on Multispectral Image Processing and Pattern Recognition, Conference on Asia Remote Sensing, and many other conferences. He edits several conference proceedings, issues, and geoinformatics symposiums. He also serves as an Associate Editor of the *International Journal of Ambient Computing and Intelligence*, *International Journal of Image and Graphics*, *International Journal of Digital Multimedia Broadcasting*, *Journal of Geospatial Information Science*, and *Journal of Remote Sensing*, and the Guest Editor of the *Journal of Applied Remote Sensing* and *Journal of Sensors*. He is currently serving as an Associate Editor of the IEEE TRANSACTIONS ON GEOSCIENCE AND REMOTE SENSING. He was a recipient of the 2010 Best Paper Boeing Award, the 2013 Best Paper ERDAS Award from the American Society of Photogrammetry and Remote Sensing (ASPRS), and the Best Reviewer Awards from the IEEE GRSS for his service to the IEEE JOURNAL OF SELECTED TOPICS IN EARTH OBSERVATIONS AND APPLIED REMOTE SENSING (JSTARS) in 2012 and IEEE GEOSCIENCE AND REMOTE SENSING LETTERS (GRSL) in 2014. His research teams won the top three prizes of the IEEE GRSS 2014 Data Fusion Contest, and his students have been selected as the winners or finalists of the IEEE International Geoscience and Remote Sensing Symposium (IGARSS) student paper contest in recent years.